

Multi-Wideband Waveform Design for Distance-Adaptive Wireless Communications in the Terahertz Band

Chong Han, *Student Member, IEEE*, A. Ozan Bicen, *Student Member, IEEE*, and Ian F. Akyildiz, *Fellow, IEEE*

Abstract—Terahertz band communication is envisioned as a key technology to satisfy the increasing demand for ultra-high-speed wireless links. In this paper, a multi-wideband waveform design for the THz band is proposed, by exploiting the channel peculiarities including the distance-varying spectral windows, the delay spread and the temporal broadening effects. This scheme allows the dynamical variation of the rate and the transmit power on each sub-window and improves the distance. Moreover, the closed-form expressions of the signal-to-interference-plus-the-noise and bit-error-rate for the multi-wideband waveform are derived, by considering the inter-symbol and inter-band interferences. Then, an optimization framework is formulated to solve for the multi-wideband waveform design parameters of the transmit power and the number of frames, with the aim to maximize the communication distance while satisfying the rate and the transmit power constraints. Four sub-optimal solutions are proposed and compared. The results show that the SINR increases with the transmit power and the number of frames, at the cost of the power consumption and the rate decrease. With the transmit power of 10 dBm, the largest distance to support 10 Gbps for the multi-path propagation is 4 m, which is realized via the power allocation scheme to minimize the power/bit on each sub-window and is 10% improvement over the fixed scheme. However, for the directional transmission, this scheme under-exploits the transmit power severely. Instead, the allocation scheme that minimizes the number of frames outperforms the other three schemes. In terms of the maximum distance that achieves 30 Gbps, this scheme reaches 22.5 m.

Index Terms—Distance-adaptive, interference, terahertz band, waveform, wideband.

I. INTRODUCTION

IN recent years, the wireless data traffic grew exponentially, which was further accompanied by an increasing demand for higher data rates [1]. Advanced physical layer solutions and, more importantly, new spectral bands will be required

Manuscript received June 21, 2015; revised October 11, 2015; accepted October 29, 2015. Date of publication November 05, 2015; date of current version January 15, 2016. The associate editor coordinating the review of this manuscript and approving it for publication was Dr. Pengfei Xia. This work was supported by the U.S. National Science Foundation (NSF) under Grant No. CCF-1349828 and in part by Alexander von Humboldt Foundation through Dr. Ian F. Akyildiz's Humboldt Research Prize in Germany. The preliminary and a much shorter version of this paper appeared in [10].

The authors are with the Broadband Wireless Networking Laboratory (BWN-Lab), School of Electrical and Computer Engineering, Georgia Institute of Technology, Atlanta, GA 30332 USA (e-mail: chong.han@ece.gatech.edu; bozan@ece.gatech.edu; ian@ece.gatech.edu).

Color versions of one or more of the figures in this paper are available online at <http://ieeexplore.ieee.org>.

Digital Object Identifier 10.1109/TSP.2015.2498133

to support these high data rates for future wireless communications. Amongst others, the (0.06–10) Terahertz band is identified as one of the promising spectrum bands to enable ultra-high-speed communications [2]. Recently, Terahertz technologies are rapidly advancing, and the development of new transceiver architectures and antennas built upon novel materials are bringing THz band communications one step closer to the reality [3]. The primary advantage of the THz band is the very broad bandwidth, which is at the order of tens of GHz depending on the transmission distance [4]. The use of this frequency band is envisioned to address the spectrum scarcity and capacity limitations of current wireless systems, and boost a plethora of applications, including ultra-high-speed wireless backhaul to the small cells, ultra-high-speed data transfers among proximal devices, and secure wireless communication for military applications [5].

The THz band communication has been a subject of study in the latest years and contributions in the literature ranging from the antenna and transceiver technologies [6], to the channel modeling [7] and MIMO techniques [8], among other communication theories. However, to the best of our knowledge, there are only few solutions which proposed on the way to design the THz signal waveform. In [9], a single-band pulse-based scheme is proposed at the THz frequencies. However, this modulation is mainly valid for very short transmission distances, e.g., nanonetworks, in which the distance-varying spectral windows do not appear. In our preliminary study, a multi-narrowband system is developed. However, the resulting number of sub-bands is quite large and the MQAM is complicated. Moreover, the interference in the multi-narrowband system is neglected [10].

For the waveform design in the THz band, the channel uniqueness needs to be best-exploited in the waveform design, which includes the distance-varying spectral windows, the large coherence bandwidth due to the delay spread and the temporal broadening effects. Hence, the waveform for transmission needs to be tailored for the channel. The additional challenges and requirements to be addressed for the THz band waveform design remain and can be summarized as follows:

- The transmission distance for ultra-high-speed communication is very limited due to the very high path loss. Moreover, the spectral windows are highly distance-dependent. Hence, an adaptive modulation scheme needs to be adopted to improve the transmission range and support ultra-high-speed links.

- The ultra-broad bandwidth of the individual spectral window at the order of tens of GHz, which motivates the multi-wideband transmission by dividing each spectral window into a set of sub-windows or sub-bands. However, the interference, including the inter-symbol and inter-band interferences of the multi-band systems, need to be investigated thoroughly and incorporated in the performance evaluation.

To address the challenges above, we propose a multi-wideband waveform design for distance-adaptive THz band communications, which can dynamically adjust the rate and the transmit power on each sub-window. In this paper, we first describe the channel characteristics of the THz band spectrum, which includes an overview of propagation model in the THz band and the characteristics. In particular, the distance-varying spectral windows, the delay spread and the temporal broadening effects are investigated. To overcome these channel impairments, we propose a multi-wideband waveform design for the distance-adaptive THz band communication, which includes the features of the pseudo-random time-hopping sequence and the polarity randomization. The carrierless version of such transmission scheme was studied for ultra-wideband communications by using a single transmission window, which optimizes the spectral shape of the transmitted signal and mitigates the inter-symbol interference [11], [12]. To cope with the unique characteristics and improve the distance, the pulse waveform design in the distance-adaptive multi-wideband system for the THz band includes the development of the waveform model and the dynamical adaptation of the rate and the transmit power on each sub-window.

Furthermore, we analyze the inter-symbol interference (ISI) between the consecutive symbols and inter-band interference (IBI) among the neighboring frequency sub-bands associated with the developed multi-wideband system, which need to be considered for the distance improvement. We further provide the close-form expressions for the signal-to-interference-plus-noise-per-bit (SINR-per-bit) and the bit-error-rate (BER) to analyze the system performance. Moreover, we formulate an optimization framework to solve for the multi-wideband waveform design parameters of the transmit power and sub-window rate (i.e., the number of frames for each symbol), based on the system model and the waveform design. The aim is to maximize the communication distance while satisfying the rate and the transmit power constraints. To avoid solving the non-convex optimization problem with the prohibitive computational complexity, four sub-optimal solutions are proposed and compared for the optimization problem. An extensive numerical analysis is performed to evaluate the multi-wideband system performance.

The remainder of this paper is organized as follows. In Section II, an overview of the THz band channel and the characteristics that affect the communication system design are described. In Section III, the multi-wideband waveform design with the associated ISI and IBI are analyzed. Moreover, the closed-form expressions for the SINR and the BER are provided in this section as well. Then, an optimization framework based on the developed waveform design for single-user communication is formulated and four sub-optimal solutions are

proposed and compared in Section IV. An extensive numerical analysis is performed to evaluate the multi-wideband system performance in Section V. Finally, the paper is concluded in Section VI.

II. TERAHERTZ BAND CHANNEL CHARACTERIZATION

In this section, we provide an overview of the THz band channel and its associated characteristics. In particular, the distance-varying spectral windows, the delay spread, and the temporal broadening effects are investigated for the THz frequencies. Based on these characteristics, we point out the design implications for the THz band communication.

A. Overview of the Terahertz Band Channel

Due to the frequency dependency appears in the propagation channel and antennas, a multi-path propagation model in the THz band is developed as the combination of many individual sub-bands in our previous work [7]. The line-of-sight (LoS) and the reflected rays are included in this multi-path model, while scattered and diffracted rays are neglected since they have insignificant contributions to the received signal power [4]. We denote t as the time and d as the communication distance. For $N_{\text{Ref}}^{(u)}$ reflected rays, the channel response of the multi-path model in the u^{th} frequency sub-band is given by

$$h_u(t, d) = \alpha_{\text{LoS}}^{(u)}(d)\delta(t - t_{\text{LoS}})\mathbb{1}_{\text{LoS}} + \sum_{q=1}^{N_{\text{Ref}}^{(u)}} \alpha_{\text{Ref}}^{(u,q)}(d)\delta(t - t_{\text{Ref}}^{(q)}), \quad (1)$$

where $\mathbb{1}_{\text{LoS}}$ is the indicator function that is equal to 1 or 0 for the presence of LoS path or not. For the LoS path, $\alpha_{\text{LoS}}^{(i)}$ refers to the attenuation, and t_{LoS} stands for the delay. For the q^{th} reflected path, $\alpha_{\text{Ref}}^{(i,q)}$ is the attenuation and $t_{\text{Ref}}^{(q)}$ is the delay. In the u^{th} frequency sub-band, the center frequency is denoted by f_u . The path loss of the channel is computed as

$$PL(f_u, d)[\text{dB}] = -20 \log_{10} |h_u(t, d)|. \quad (2)$$

The total number of multi-path components is given by $N_u = \mathbb{1}_{\text{LoS}} + N_{\text{Ref}}^{(u)}$, with $N_{\text{Ref}}^{(u)} < 10$ [7]. On the one hand, the THz band transmission is omni-directional and the multi-path signal consists of the LoS and multiple reflected paths, when the gains of the transmitting and receiving antennas are $G_t = G_r = 0$ dBi. On the other hand, with the use of high-gain antenna or very large antenna arrays to overcome the very high path loss, the number of multi-path rays and the delay spread decrease, while the total received signal power increases. In particular, when the gains of the transmitting and receiving antennas are $G_t = G_r = 20$ dBi, the THz band transmission is highly directional and the number of multi-path components reduces to a small number, i.e., $N_u = 1$ [10].

B. Distance-Varying Spectral Windows

To analytically characterize the distance-varying spectral windows, we further define the *path loss threshold*, PL_{th} . The spectrum that has smaller path loss than this threshold forms

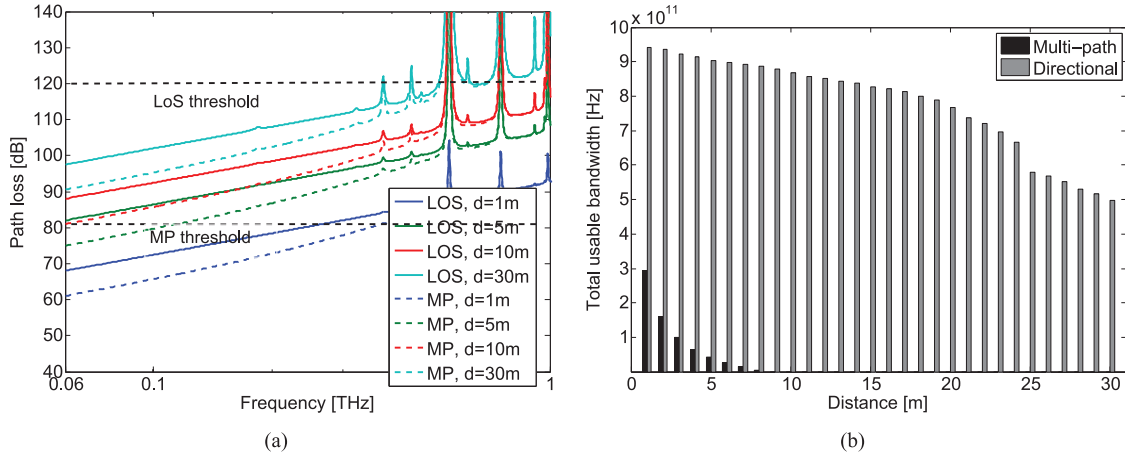


Fig. 1. Distance-varying path loss and total usable bandwidth for multi-path and directional transmissions in the THz band. (a) Path loss. (b) Total usable bandwidth.

TABLE I
PHYSICAL PARAMETERS USED IN THIS PAPER

Notation	Parameter Definition	Value	Unit
P_{Tx}	Transmit power	10	dBm
G_t	Transmit antenna gain	[0, 20]	dBi
G_r	Receive antenna gain	[0, 20]	dBi
γ_{th}	Minimum SINR-per-bit	10	dB
P_w	Noise and interference power	-80	dBm
T_p	Pulse duration	0.5	ns
N_p	Number of pulse positions in one frame	5	-
T_f	Frame duration	2.5	ns
N_f^u	Number of frames for one symbol	[1, 10]	-
B_g	Sub-window bandwidth	10	GHz
N_u	Number of multi-path components	[1, 5]	-

the spectral windows. This path loss threshold is computed by invoking the link budget equation, as

$$PL_{th} = P_{Tx} + G_t + G_r - \gamma_{th} - P_w, \quad (3)$$

where P_{Tx} refers to the transmit power, γ_{th} stands for the minimum SINR, and P_w represents the noise and interference power. The parameter values used in this paper are listed in Table I [13]. Using this threshold, we determine the spectral windows and the total usable bandwidth in the THz Band for the different transmission cases.

1) *Spectral Windows for $G_t = G_r = 0$ dBi*: In the multi-path propagation model, we consider the received signal is a superposition of the LoS and four reflected paths, over the frequency band 0.06 to 1 THz, where the material parameters are readily available [7]. Additionally, the reflection loss grows drastically as the frequency becomes very large, so that the high frequency bands (above 1 THz) apparently do not satisfy the path loss threshold. The path loss values for the different distances are shown in Fig. 1(a), where the path loss threshold in this case is equal to 80 dB. The communication distance is limited for multi-path propagation based on this threshold. At the distance above 8 m, there is no usable spectrum in the THz band. Below 8 m, the total usable bandwidth is illustrated in Fig. 1(b), which is equal to 0.29 THz at $d = 1$ m. The decreasing rate from $d = 1$ m to 8 m is 40.91 GHz/m.

2) *Spectral Windows for $G_t = G_r = 20$ dBi*: With high antenna gains, the transmission is directional through the LoS

path in one narrowbeam. The path loss in the THz Band for different distances are shown in Fig. 1(a). From (3), the path loss threshold equals to 120 dB. The path loss peaks caused by the molecular absorption create spectral windows, which have different bandwidth, and drastically change with the variation of the distance. A few path loss peaks appear over this frequency band, such as at 0.56 THz, 0.75 THz, and 0.98 THz, and the number of peaks increases with the distance. According to this threshold value, the total bandwidth over the THz spectrum is identified in Fig. 1(b), for the different separation distance. For example, the total bandwidth over the 0.06–1 THz band shrinks from 0.94 THz, 0.90 THz, 0.87 THz to 0.50 THz, when the distance rises from 1 m, 5 m, 10 m to 30 m. The decreasing rate of the total usable bandwidth from 1m to 30 m this range is approximately 14.7 GHz/m.

C. Delay Spread and Temporal Broadening

In the multi-path channel, the delay spread is a measure of how dispersive the channel is, which reduces as the antenna directivity increases. This temporal parameter relates to the performance degradation caused by ISI and useful for the physical system design. Moreover, the coherence bandwidth, that is defined as the range of frequencies over which channel correlation exceeds 50%, is given by $0.2/\sigma_u$ where σ_u refers to the rms delay spread of the multi-path channel. Due to the decrease of the beamwidth in the directional antenna case, the number of significant multi-path components decreases. Hence, the rms delay spread reduces by more than a factor of 60 when the directional antenna is used. For example, at $f = 0.3$ THz and $d = 5$ m, The coherence bandwidth for the multi-path propagation is 1 GHz, and it reaches over 60 GHz when the directional antenna is used [14]. This indicates a very large range of frequencies over which the channel can be considered as flat.

In addition to the delay spread, the temporal broadening effects describe the broadening on the transmitted pulses, when they experience the frequency-selectivity in the THz wideband channel. The frequency-selective attenuation causes broadening effects on the transmitted signals, which restricts the minimum spacing between consecutive pulses and results in additional coherence bandwidth. The broadening effects

increase for the higher center frequency, the wider pulse bandwidth and the longer communication distance, since the level of frequency-selectivity in the channel increases under these variations. Moreover, the reflected propagation affects the temporal broadening, since the reflection introduces additional loss as well as distortion on the transmitted signals, particularly at higher frequencies. If we define the broadening factor as the ratio between the pulse duration of the received pulse and that of the transmitted pulse, this factor at the THz frequencies is found to be 5, when the pulse bandwidth is below 10 GHz. This indicates that the received pulse becomes 5 times as wide as the transmitted pulse.

D. Design Guidelines

The design guidelines based on the channel characteristics are highlighted as follows. The very strong relationship between the distance and the spectral windows at THz frequencies motivates the design to be distance-adaptive and in the form of multi-wideband. According to the link budget analysis in (2), the guide of the total usable bandwidth is provided. Moreover, the utilization of the sub-bands needs to be intelligently selected to avoid spectrum with the path loss peaks. Specifically, in the multi-path propagation with $d = 5$ m, the spectrum above 0.1 THz has significantly large path loss and cannot be used. In the directional propagation, the communication around 0.56 THz, 0.75 THz, and 0.98 THz needs to be prevented.

In terms of the transmission over each sub-band, wideband pulses can be used, for the features of ultra-low power, compact-size and ultra-low complexity design. These pulses were firstly proposed for ultra-wideband communication [11] and then was tailored for THz band communication [9]. By occupying the bandwidth B_g , each sub-window experiences frequency-selective fading for multi-path propagation, while undergoes flat-fading for directional transmission with a much larger coherence bandwidth, as discussed in Section II-C. Furthermore, in accordance with the temporal broadening, the minimum separation between the consecutive pulses to avoid the pulse overlapping is $5T_p$, where T_p denotes the pulse waveform duration.

III. MULTI-WIDEBAND COMMUNICATIONS IN THE TERAHERTZ BAND

In this section, we first propose a multi-wideband waveform model for the distance-adaptive THz band communication by exploiting the channel peculiarities. Furthermore, we analyze the inter-symbol interference (ISI) between the consecutive symbols and inter-band interference (IBI) among the neighboring frequency sub-bands associated with the developed multi-wideband system. We further provide the close-form expressions for the signal-to-interference-plus-noise-per-bit (SINR-per-bit) and the bit-error-rate (BER) to analyze the system performance.

A. Pulse Waveform Model

In the multi-wideband communication, each sub-window experiences frequency-selective fading, since the width of the sub-window is greater than the coherence bandwidth, as studied in the previous section. To combat the frequency selective

fading and increase the received SINR-per-bit, each information symbol on the sub-window is represented by a sequence of very short pulses, which provides the pulse combing gain [11]. Within one sequence, the positions of the pulses are determined by a pseudo-random time-hopping sequence that is specific to each sub-window. Furthermore, pulse-based polarity randomization is utilized to provide further robustness against the interference and help optimize the spectral shape, which was studied for ultra-wideband communications in [11], [12]. We tailor this pulse waveform to the THz band to cope with the unique characteristics at the THz frequencies and improve the SINR or equivalently, the distance.

For the transmission on the u^{th} sub-window, the baseband signal consists of different symbols. For the i^{th} information symbol, N_f^u frames are used to describe this symbol with one pulse in one frame. This is represented as

$$x_u(t) = \sqrt{P_u} \sum_i a_u^{(i)} \sum_{m=0}^{N_f^u-1} p_u^{(i,m)} \cdot g(t - iN_f^u T_f - mT_f - c_u^{(i,m)} T_p), \quad (4)$$

where T_f and T_p denote the time duration for one frame and one pulse, with their ratio defining the number of pulse positions in a frame, i.e., $N_p = T_f/T_p$. Additionally, P_u stands for the allocated power in the u^{th} sub-window, N_f^u is the number of frames to represent one information symbol. In the signal model with polarity randomization and time hopping, $a_u^{(i)} \in \{+1, -1\}$ is the i^{th} binary information symbol, $p_u^{(i,m)}$ denotes the random polarity code that takes ± 1 with equal probability, and $c_u^{(i,m)}$ refers to the time hopping code where $c_u^{(i,m)} \in \{0, 1, \dots, N_p - 1\}$ with equal probability of the m^{th} frame. $g(t)$ is the transmitted wideband pulse with the duration T_p and unit energy.

By combining the signal model in (4) and the THz band channel model in (1), the received signal is described as

$$\begin{aligned} y_u(t, d) &= x_u(t) * h_u(t, d) + w(t) \\ &= \alpha_{\text{LoS}}^{(u)}(d) \sqrt{P_u} \sum_i a_u^{(i)} \sum_{m=0}^{N_f^u-1} p_u^{(i,m)} \\ &\quad \cdot g_r(t - iN_f^u T_f - mT_f - c_u^{(i,m)} T_p - t_{\text{LoS}}) \mathbb{1}_{\text{LoS}} \\ &\quad + \sqrt{P_u} \sum_{q=1}^{N_{\text{Ref}}^{(u)}} \alpha_{\text{Ref}}^{(u,q)}(d) \sum_i a_u^{(i)} \sum_{m=0}^{N_f^u-1} p_u^{(i,j)} \\ &\quad \cdot g_r(t - iN_f^u T_f - mT_f - c_u^{(i,m)} T_p - t_{\text{Ref}}^{(q)}) + w(t) \\ &= \sqrt{P_u} \sum_i a_u^{(i)} \sum_{m=0}^{N_f^u-1} p_u^{(i,m)} \\ &\quad \cdot \psi_u(t - iN_f^u T_f - mT_f - c_u^{(i,m)} T_p) + w(t), \quad (5) \end{aligned}$$

where $w(t)$ is the Gaussian noise with the power spectral density S_w , and we define

$$\psi_u(t) = \alpha_{\text{LoS}}^{(u)}(d) g_r(t - t_{\text{LoS}}) \mathbb{1}_{\text{LoS}} + \sum_{q=1}^{N_{\text{Ref}}^{(u)}} \alpha_{\text{Ref}}^{(u,q)}(d) g_r(t - t_{\text{Ref}}^{(q)}), \quad (6)$$

with $\boldsymbol{\alpha}^{(u)} = [\alpha_{\text{LoS}}^{(u)}, \alpha_{\text{Ref}}^{(u,1)}, \dots, \alpha_{\text{Ref}}^{(u, N_{\text{Ref}}^u)}]$, and g_r is the received pulse with the unit energy, which includes the THz band channel effects on g , as defined in (4).

To combine the multi-path signals for the u^{th} sub-window, a Rake receiver is used with $\boldsymbol{\beta}^{(u)} = [\beta_{\text{LoS}}^{(u)}, \beta_1^{(u)}, \dots, \beta_{N_{\text{Ref}}}^{(u)}]$ being the Rake combining weights.

The output of the Rake receiver for the i^{th} binary information symbol can be obtained in the form of

$$r_u^{(i)}(d) = a_u^{(i)} \sqrt{P_u} N_f^u \alpha_{\text{LoS}}^{(u)}(d) \beta_{\text{LoS}}^{(u)} \mathbf{1}_{\text{LoS}} + a_u^{(i)} \sqrt{P_u} N_f^u \sum_{q=1}^{N_{\text{Ref}}^{(u)}} \alpha_{\text{Ref}}^{(u,q)}(d) \beta_q^{(u)} + ISI_u + IBI_u + w_u, \quad (7)$$

where the first term is due to the desired signal propagating through the LoS path, the second term is from the desired signals through the reflected paths, the third term is the ISI from the pulses in the adjacent frames due to the multi-path and temporal broadening effects, the fourth term describes the IBI from the surrounding sub-windows, and the last term refers to the output noise.

In particular, the parameters in the multi-wideband waveform design in (4) include the transmit power and the number of frames. Moreover, these parameters interact with each other and will be investigated in-depth in Section IV.

B. Interference

We analyze the two types of interference associated with the multi-wideband transmission as described in the previous section, namely, ISI and IBI, which account for the interference effects among different symbols and different sub-windows.

1) *Inter-Symbol Interference (ISI)*: The interference for the i^{th} information symbol can be obtained as a sum of the interference effects on the individual pulses that consist of this symbol

$$ISI_u = \sqrt{P_u} \sum_{m=iN_f^u}^{(i+1)N_f^u-1} I_u^{(i,m)}, \quad (8)$$

where the interference on the m^{th} pulse, $I_u^{(i,m)}$, is

$$I_u^{(i,m)} = p_u^{(i,m)} \sum_{n_1}^{N_f^u-1} \sum_{n_2=0}^{N_f^u-1} p_u^{(n_1, n_2)} a_u^{(n_1)} \Psi_u \left[(n_1 - i) N_f^u T_f + (n_2 - m) T_f + (c_u^{(n_1, n_2)} - c_u^{(i, m)}) T_p \right]. \quad (9)$$

Note that when $n_1 = i, n_2 = m$, $\Psi_u(0) = 0$. In the above equation, Ψ_u represents the cross-correlation between ψ_u and ψ'_u , as

$$\Psi_u(\tau) = \int_{-\infty}^{+\infty} \psi_u(t - \tau) \psi'_u(t) dt, \quad (10)$$

where ψ_u is given in (6), ψ'_u represents the weighted sum of the delayed version of the received pulse, in the form of

$$\psi'_u(t) = \beta_{\text{LoS}}^{(u)}(d) g_r(t - t_{\text{LoS}}) \mathbf{1}_{\text{LoS}} + \sum_{q=1}^{N_{\text{Ref}}^{(u)}} \beta_q^{(u)}(d) g_r(t - t_{\text{Ref}}^{(q)}) \quad (11)$$

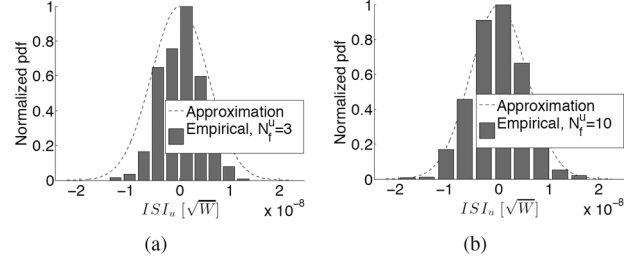


Fig. 2. Probability density function of the ISI amplitude, in comparison with the empirical realizations. (a) $N_f^u = 3$. (b) $N_f^u = 10$.

where the weights are the Rake receiver coefficients. The expected value of the interference is equal to zero due to the random polarity code that takes ± 1 with equal probability. The variance can be calculated from (9) and (10), as

$$E \left[I_u^{(i,m)^2} \right] = \frac{1}{N_p^2} \sum_{m=1}^{N_u-1} m \left[\sum_{l=1}^{N_u-m} R_{g_r}(mT_p) \left(\boldsymbol{\beta}^{(u)}(l) \boldsymbol{\alpha}^{(u)}(l+m) + \boldsymbol{\alpha}^{(u)}(l) \boldsymbol{\beta}^{(u)}(l+m) \right) \right]^2 \quad (12)$$

where $\boldsymbol{\alpha}^{(u)}$ is the vector of the channel attenuations and $\boldsymbol{\beta}^{(u)}$ is the vector of the Rake receiver weights, as defined in Section III-A. R_{g_r} denotes the auto-correlation function of g_r in (5).

In light of the results in (8) and (12), ISI_u for the multi-path propagation is approximately distributed as

$$ISI_u \sim \mathcal{N} \left(0, \frac{P_u}{N_p^2} \sum_{m=1}^{N_u-1} m \left[\sum_{l=1}^{N_u-m} R_{g_r}(mT_p) \left(\boldsymbol{\beta}^{(u)}(l) \boldsymbol{\alpha}^{(u)}(l+m) + \boldsymbol{\alpha}^{(u)}(l) \boldsymbol{\beta}^{(u)}(l+m) \right) \right]^2 \right). \quad (13)$$

In (9), $p_u^{(i,m)}$ denotes the random polarity code and $a_u^{(i)}$ is the i^{th} binary information symbol, which both take ± 1 with equal probability, as defined in Section III-A. Moreover, the channel response in the u^{th} sub-window in (1) as a function of the distance, the Rake receiver coefficients and the number of frames are included in this expression. Figs. 2(a) and 2(b) depict the probability density function (pdf) of the ISI amplitude, for $N_f^u = 3$ and 10. The approximation in (13) shows a good agreement with the empirical realizations of ISI_u . As N_f^u increases, the accuracy of the approximation improves.

As the distance increases, the delay spread and the temporal broadening effects increase. However, the increase of the distance reduces the path gains, particularly of the reflected paths since they travel through additional distances and suffer from the reflection loss. Hence, the resulting ISI becomes weaker. The above analysis for the ISI is for the multi-path propagation. With the use of high-gain antennas, the beamwidth of the transmission is small and the number of the multi-path components reduces drastically. As studied in Section II-C, the delay spread with the 20-dB-gain antennas is negligible with $N_u = 1$. Furthermore, the temporal broadening effects are reduced thanks to the smaller path loss and frequency selectivity in the channel.

Hence, the ISI effects can be neglected in the directional transmission.

2) *Inter-Band Interference (IBI)*: The inter-band interference occurs in the multi-wideband systems which causes from the power leakage from the neighboring sub-windows. In the THz band, the number of sub-windows is at the order of multiple-tens. To model this interference, we invoke the central limit theorem to approximate the IBI with a Gaussian process. The IBI accounts for the power leakage from the surrounding sub-windows. It is shown in [15]–[17] that the interference from the adjacent frequency bands can be approximated as Gaussian distributed random variable. Hence, the distribution of the interference power on the u^{th} sub-window that superimposes from the other sub-windows has the expression

$$\begin{aligned} IBI_u &\sim \\ \mathcal{N} &\left(0, \int_{f_u} \sum_{v, v \neq u}^{U(d)} P_v |G_r^v(f_u)| \sum_{m=1}^{N_u} \alpha^{(v)}(m) \beta^{(v)}(m) df_u\right), \\ &\approx \mathcal{N}\left(0, P_u \int_{f_u} \sum_{v, v \neq u}^{U(d)} |G_r^v(f_u)| \sum_{m=1}^{N_u} \alpha^{(v)}(m) \beta^{(v)}(m) df_u\right), \end{aligned} \quad (14)$$

where $G_r^v(f_u)$ describes the interference on the u^{th} sub-window that is contributed from the v^{th} sub-window, with $v \neq u$.

The IBI mainly contributes from the neighboring sub-windows, i.e., $(u+1)^{\text{th}}$ and $(u-1)^{\text{th}}$ in this case. Hence, we rearrange the IBI_u by using P_u in the above approximation, by considering the channel quality and the resulting transmit power for the neighboring sub-windows are similar. This approximation is useful to obtain P_u in (20). Moreover, G_r^v is the frequency response from the v^{th} sub-window, based on the received pulse g_r in (5). The interaction with the THz band channel and the receiver coefficients are also captured in the above expression, which influences the IBI.

The IBI captures the power leakage from the surrounding sub-windows, and increases if the separation between the consecutive sub-windows (i.e., the bandwidth of the sub-window that is denoted by B_g) decreases. As the distance increases, the frequency selectivity becomes more severe. Consequently, the temporal broadening makes the transmitted pulse in the time domain wider, which thereby leads to a reduction of the IBI in the frequency domain. With the use of high-gain antennas, the delay spread reduces significantly and the channel frequency response varies less frequency-selective. However, the path loss of the channel is reduced and hence, the IBI becomes more significant in this case. These effects are captured in (14).

C. Signal-to-Interference-Plus-Noise-Ratio-Per-Bit (SINR-per-bit)

The noise based on the Rake receiver in (7) is the weighted sum of the Gaussian noise from the different paths. The power spectral density of the noise is distributed as

$$w_u \sim \mathcal{N}\left(0, N_f^u S_w \sum_{l=1}^{N_u} [\beta^{(u)}(l)]^2\right). \quad (15)$$

Hence, by combining (7), (13), (14) and (15), the SINR-per-bit in the u^{th} sub-window at the receiver is calculated as

$$\gamma_u^{\text{mp}}(d) = \frac{P_u \left[N_f^u \left(\alpha_{\text{LoS}}^{(u)}(d) \beta_{\text{LoS}}^{(u)} \right) + N_f^u \sum_{q=1}^{N_{\text{Ref}}^{(u)}} \left(\alpha_{\text{Ref}}^{(u,q)}(d) \beta_q^{(u)} \right) \right]^2}{\frac{P_u}{N_p^2} \sigma_{\text{ISI}}^2 + P_u \sigma_{\text{IBI}}^2 + B_g N_f^u S_w \sigma_{\text{noise}}^2}, \quad (16)$$

where the interference and noise terms in the above equation are stemmed from (13), (14), and (15), respectively

$$\sigma_{\text{ISI}}^2 = \sum_{m=1}^{N_u-1} m [R_{g_r}(mT_p) \sum_{l=1}^{N_u-m} (\beta^{(u)}(l) \alpha^{(u)}(l+m) + \alpha^{(u)}(l) \beta^{(u)}(l+m))]^2, \quad (17)$$

$$\sigma_{\text{IBI}}^2 = \int_{f_u} \sum_{v, v \neq u}^{U(d)} |G_r^v(f_u)| \sum_{m=1}^{N_u} \alpha^{(u)}(m) \beta^{(u)}(m) df_u, \quad (18)$$

$$\sigma_{\text{noise}}^2 = \sum_{l=1}^{N_u} [\beta^{(u)}(l)]^2. \quad (19)$$

Correspondingly, for a given SINR-per-bit and the number of frame, the required transmit power on the sub-window is given by

$$P_u = \frac{\gamma_u^{\text{mp}}(d) B_g N_f^u S_w \sigma_{\text{noise}}^2}{\left[N_f^u \left(\alpha_{\text{LoS}}^{(u)}(d) \beta_{\text{LoS}}^{(u)} \right) \mathbf{1} + N_f^u \sum_{q=1}^{N_{\text{Ref}}^{(u)}} \left(\alpha_{\text{Ref}}^{(u,q)}(d) \beta_q^{(u)} \right) \right]^2 - A_1} \quad (20)$$

where $A_1 = \gamma_u^{\text{mp}}(d) \left[\frac{\sigma_{\text{ISI}}^2}{N_p^2} + \sigma_{\text{IBI}}^2 \right]$.

The above analysis for the ISI is for the multi-path propagation with $G_t = G_r = 0$ dB. With the use of high-gain antennas, the transmission becomes directional and consequently, $N_u = 1$ and $\alpha_{\text{LoS}}^{(u)} \neq 0$. Moreover, the ISI term becomes negligible while the IBI term becomes more important. The SINR-per-bit for the directional transmission, γ_u^{di} , is given by

$$\gamma_u^{\text{di}}(d) = \frac{\left(N_f^u \alpha_{\text{LoS}}^{(u)}(d) \beta_{\text{LoS}}^{(u)} \right)^2}{\int_{f_u} \sum_{v, v \neq u}^{U(d)} |G_r^v(f_u)| \alpha_{\text{LoS}}^{(u)}(d) \beta_{\text{LoS}}^{(u)} df_u + \frac{B_g N_f^u S_w}{G_t G_r P_u} \left[\beta_{\text{LoS}}^{(u)} \right]^2}. \quad (21)$$

As a function of the desired SINR, the required transmit power on the sub-window for the directional transmission is

$$P_u^{\text{di}} = \frac{\gamma_u^{\text{di}}(d) B_g N_f^u S_w \left[\beta_{\text{LoS}}^{(u)} \right]^2}{G_t G_r \left(N_f^u \alpha_{\text{LoS}}^{(u)}(d) \beta_{\text{LoS}}^{(u)} \right)^2 - A_2} \quad (22)$$

where

$$A_2 = \gamma_u^{\text{di}}(d) \int_{f_u} G_t G_r \sum_{v, v \neq u}^{U(d)} |G_r^v(f_u)| \alpha_{\text{LoS}}^{(u)}(d) \beta_{\text{LoS}}^{(u)} df_u.$$

D. Bit-Error-Rate (BER)

In light of the SINR for the designed multi-wideband waveform, the error performance of the system can be computed. Particularly for the pulse-based systems by incorporating the interference and the noise effects jointly, the Q-function of the SINR was shown to capture the error behavior [11], [18]–[20].

Hence, starting with the SINR expression in (16), the BER over the u^{th} sub-window for the multi-path propagation can be approximated as

$$\begin{aligned} \epsilon_u^{\text{mp}} &\approx Q(\sqrt{\gamma_u^{\text{mp}}}) \\ &\approx Q\left(\frac{N_f^u \alpha_{\text{LoS}}^{(u)}(d) \beta_{\text{LoS}}^{(u)} + N_f^u \sum_{q=1}^{N_{\text{Ref}}^{(u)}} \alpha_{\text{Ref}}^{(u,q)}(d) \beta_q^{(u)}}{\sqrt{\frac{A_1}{\gamma_u^{\text{mp}}(d)} + B_g N_f^u S_w \sigma_{\text{noise}}^2 / P_u}}\right), \end{aligned} \quad (23)$$

where $Q(\cdot)$ denotes the Q-function.

For the directional transmission, the ISI can be omitted while the IBI increases with the use of high-gain antennas. According to the SINR expression in (21), the BER over one sub-window is given in the similar fashion, as

$$\epsilon_u^{\text{di}} \approx Q\left(\frac{\sqrt{G_t G_r P_u N_f^u \alpha_{\text{LoS}}^{(u)}(d) \beta_{\text{LoS}}^{(u)}}}{\sqrt{\frac{A_2 P_u}{\gamma_u^{\text{di}}(d)} + B_g N_f^u S_w [\beta_{\text{LoS}}^{(u)}]^2}}\right). \quad (24)$$

From the above equations, the BER decreases with the increase of the SINR. Consequently, the BER decreases with the increase of the transmit power and the number of frames. Moreover, the BER in the directional transmission is greatly reduced thanks to the additional antenna gains as well as the elimination of the ISI.

IV. MULTI-WIDEBAND WAVEFORM DESIGN

To cope with the unique characteristics in Section II and improve the distance, we dynamically adapt the rate (i.e., the number of frames) and the transmit power on each sub-window in the pulse waveform model of the distance-adaptive multi-wideband system in (4). To solve for these parameters, we formulate and solve the optimization framework with the aim to maximize the distance while satisfying the rate and transmit power constraints. Noticeably, this problem can be solved by solving the rate maximization problem for a given distance iteratively, by which the maximum distance is obtained when the maximum rate in the first problem reaches the threshold, R_{th} . In this section, we present the problem formulation and the solution to these two problems.

A. Rate Maximization for the Fixed Distance

For a distance d , we consider the total number of sub-windows is $U(d)$, which is the ratio between the total usable bandwidth (see Fig. 1(b)) and the sub-window bandwidth, B_g . The total rate is equal to the sum of the rate over each sub-window, as

$$R_{\text{tot}} = \sum_{u=1}^{U(d)} k_u, \quad (25)$$

where by using the wideband signal model in (4), the rate over the u^{th} sub-window is equal to the inverse of the number of the symbols in one second, which is given by

$$\begin{aligned} k_u &= \frac{1}{N_f^u N_p T_p} \\ &= \frac{1}{N_f^u T_f}. \end{aligned} \quad (26)$$

The computation of k_u is a function of the number of frames. The number of frames is included in the SINR-per-bit in (16) and (21), for the multi-path and directional propagations, respectively. Moreover, the BER, in (23) and (24), are functions of the SINR-per-bit and the computed k_u . Therefore, k_u takes the SINR-per-bit as well as the BER into account implicitly. In fact, a tradeoff as an outcome of the waveform design is that the increase of the number of frames leads the decrease of the rate, the increase of the SINR-per-bit, and the decrease of the BER.

According to the waveform design in Section III-A, when $N_f^u = 1, \forall u = 1, \dots, U(d)$ is the theoretical upper bound to the data rate. However, this solution is infeasible due to the constraints on the transmit power and the SINR. To maximize the rate, the transmit power, P_u , and the number of frames, N_f^u , need to be determined over each sub-window. As the power needed to achieve a certain rate on one sub-window is independent of the rates on other sub-windows, we decouple the allocation of the transmit power with the distribution of the number of frames to obtain a sub-optimal solution. Furthermore, the spectral windows that are used for transmission are distance-adaptive and in particular, the sub-windows whose path loss exceeds the path loss threshold are not used (see Section II-B). After the transmit power allocation is accomplished, the number of frames on each sub-window, N_f^u , can be determined as the smallest number that fulfills the SINR requirement. In particular, four power allocation schemes are considered in our analysis, as follows.

- 1) *Min power/bit*: The first scheme allocates the transmit power by minimizing the power-per-bit, which is also suggested in [21]. Relating to our waveform design, this scheme targets to minimize power/bit for each sub-window, i.e., minimize $P_u \cdot N_f^u$ as the rate is inversely proportional to N_f^u . This scheme allows an effective and fair utilization of the transmit power. The resulting power allocation increases steadily as the frequency increases and the SINR decreases. The resulting allocation is equivalent to the power inversion scheme, where more power is allocated to the higher frequency bands.
- 2) *Min N_f^u* : The second scheme allocates the power starting from the lower frequencies, i.e., $f_1 = 0.06$ THz to $f_U = 1$ THz, due to the monotonic increase of the path loss values, as shown in Section II-B. At each sub-window, the transmit power satisfies the SINR requirement with the lowest possible N_f^u , i.e., $N_f^u \geq 1$. This allocation continues until the transmit power requirement in (30) is satisfied. This may result in an unfair utilization of the transmit power by allocating no power to the high THz frequencies. This scheme is equivalent to the truncated power inversion scheme in [22].
- 3) *Water-filling*: The third scheme follows the water-filling principle [22], which results in the fact that the sub-windows with better quality are distributed with more power. To implement the water-filling allocation scheme, the SINR on each sub-window in (16) is computed by assuming the same number of frames, for example, $N_f^u = 1$. After the power distribution is determined, the smallest N_f^u is computed for each sub-window to achieve the possible largest rate.

4) *Equal-power*: The fourth scheme follows the equal-power principle [22], by letting $P_u = P_{\text{Tx}}$. Then, the smallest N_f^u is computed for each sub-window. This scheme allows the transmit power and the number of frames to be obtained offline and greatly reduces the computational complexity.

The complexities of sub-optimal algorithms are significantly reduced since the allocation of the transmit power is decoupled with the distribution of the number of frames, i.e., the rates over each sub-window. The four schemes yield different system performance as well as the computational complexity. The rate performance and the operation regions of the four schemes are investigated in the numerical section in Section V, for both the multi-path propagation and the directional transmission, as studied in Section II.

B. Distance Maximization

In the previous section, the maximal rate is obtained for a given distance and the constraints on the transmit power and the SINR-per-bit. In light of these results, we formulate an optimization to find the largest distance by solving the previous problem iteratively, by which the maximum distance is obtained when the maximum rate in the first problem reaches the threshold, R_{th} .

1) *Optimization Framework Formulation*: For the multi-wideband system in the THz band, we formulate an optimization problem to maximize the communication distance, d , as follows:

$$\text{Given: } P_{\text{Tx}}, \gamma_{\text{th}}, R_{\text{th}}, S_w$$

$$\text{Find offline: } T_f, T_p, N_p, B_g, \beta^u \geq 0 \quad (27)$$

$$\text{Find: } N_f^u, P_u \geq 0, \quad (28)$$

$$\text{Maximize: } d \quad (29)$$

Subject to:

$$\text{Transmit power: } E[P_u] \leq P_{\text{Tx}} \quad (30)$$

$$\text{SINR-per-bit: } \gamma_u^{\text{mp}}(d) \geq \gamma_{\text{th}}, \forall u = 1, \dots, U(d) \quad (31)$$

$$\text{Data rate: } \sum_{u=1}^{U(d)} \frac{1}{N_f^u N_p T_p} \geq R_{\text{th}}. \quad (32)$$

In the above framework, $E[\cdot]$ stands for the expectation operator. Moreover, U denotes the total number of sub-windows at the distance d with the sub-window bandwidth B_g , which is at the order of 10^2 . In (31), γ_u^{mp} is given in (16). In (32), the data rate is obtained from (26).

2) *Solution to the Optimization Problem*: This optimization requires prohibitive computational complexity for an optimal solution, for the following reasons. First, this is a non-convex optimization problem with a non-convex constraint (32), since the Hessian of this constraint is not positive semi-definite.

Furthermore, the complexity grows exponentially with the number of constraints and variables. There are $U+2$ constraints and the number of variables is $2U$, where U is at the order of 10^2 . Instead of searching for an optimal solution, we use algorithms developed in Section IV-A to obtain the sub-optimal solutions for the design parameters. Initially, we select the Rake receiver coefficients by pursuing the maximum ratio combining principle. The amplitude and the phase satisfy [23]

$$\beta_l^{(u)} = |\alpha_l| e^{j2\pi f_u t_l}, \text{ for } l = 1, \dots, N_u. \quad (33)$$

Moreover, we compute the pulse width, $T_p = 0.5$ ns, the number of pulse positions in one frame, $N_p = 5$, and the bandwidth of the sub-window, $B_g = 10$ GHz, to satisfy the THz channel peculiarities as shown in Table I, which are common for all the sub-windows. Particularly, the separation between the consecutive pulses N_p needs to sufficiently large to avoid the temporal broadening effects, and the selection of the spectral windows at any distance to satisfy the link budget equation in (3).

So far the offline parameters of the optimization problem in (29) have been obtained. Next, the distance maximization problem is addressed by solving the rate maximization problem for a given distance iteratively, by which the maximum distance is obtained when the maximum rate reaches the threshold. The detailed solution to the rate maximization problem is detailed in Section IV-A, in which the power allocation and the rate assignment are decoupled. In particular, four power allocation schemes are considered in our analysis, namely, min power/bit, min N_f^u , water-filling and equal-power. Based on these power allocation schemes, the number of frames on each sub-window can be obtained, which completes the solution of the distance maximization problem.

C. Design Tradeoffs

The channel peculiarities and the multi-wideband waveform design are fully captured in the optimization problem. In particular, the SINR-per-bit in (31) and the data rate in the constraint (32) are obtained based on the functions of the channel in (1), the waveform signal in (4), and the interferences in (13) and (14).

The optimization problem has two variables that appear in the waveform signal in (4) and are closely interacted with each other, which are: the transmit power, P_u , and the number of frames, N_f^u , over each sub-window, which The number of frames can also be understood as the rate computation over each sub-window. The increase of the transmit power allows a smaller number of frames in one sub-window to satisfy the SINR-per-bit constraint. This consequently increases the rate on that particular sub-window. However, the relationship between the transmit power and the data rate on one sub-window is not linear. Moreover, increasing the transmit power in one sub-window suggests a reduction of the available power to other sub-windows. From another perspective, large numbers of frames on the sub-windows require less power to fulfill the SINR-per-bit constraint. Although the rate over each sub-window is reduced, more sub-windows can be utilized in this case.

To increase the communication distance and the rate over the THz band, the tradeoff between the transmit power and the number of frames on the sub-windows, that are realized in the four allocation schemes in Section IV-A, need to be investigated thoroughly. Furthermore, the impact of the propagation peculiarities in the THz band such as the antenna gains, path gains, the delay spread and the temporal broadening influence the wideband waveform design and ultimately the THz system performance. Lastly, the complexity of this algorithm is significantly reduced since the allocation of the transmit power is decoupled

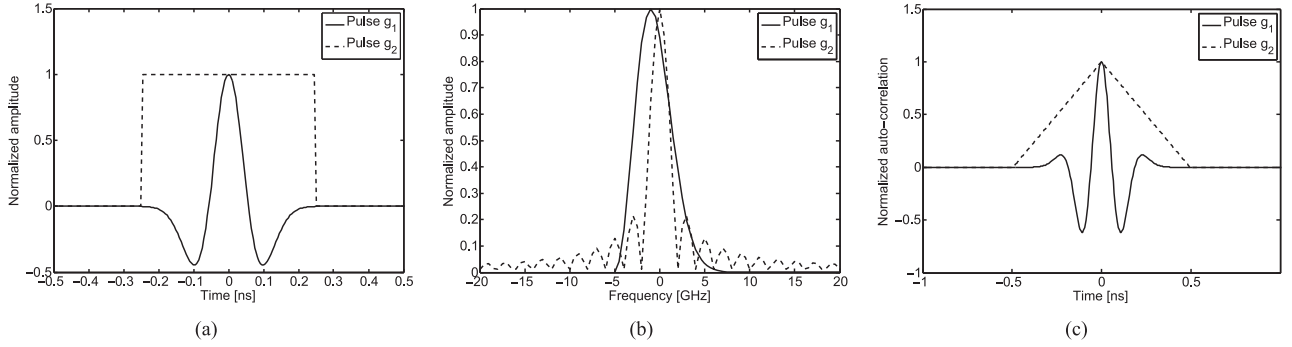


Fig. 3. The wideband THz pulse waveform properties. (a) Time response. (b) Frequency response. (c) Auto-correlation function.

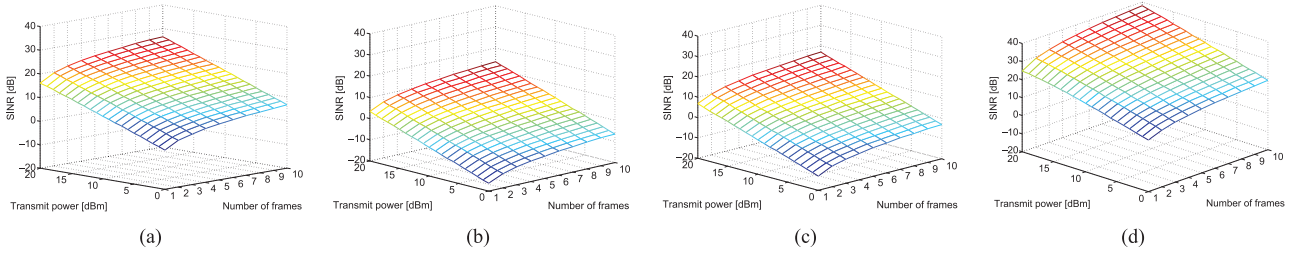


Fig. 4. SINR for the different distances and frequencies. (a) Multi-path propagation with $d = 5$ m, $f = 60$ GHz. (b) Multi-path propagation with $d = 5$ m, $f = 300$ GHz. (c) Multi-path propagation with $d = 1$ m, $f = 1$ THz. (d) Directional transmission with $d = 30$ m, $f = 300$ GHz.

with the distribution of the number of frames, i.e., the rates over each sub-window.

V. NUMERICAL ANALYSIS

In this section, we perform numerical analysis on the multi-wideband waveform design for the multi-path propagation and directional transmission, respectively. In particular, the SINR and the BER for the different transmit power, the different number of frames, and the different waveforms are studied. By using the THz band channel and the waveform design, the rate is analyzed, which is dependent on the transmit power, the communication distance, and the power allocation scheme. Finally, the improvement of the distance to achieve the data rate requirement, R_{th} , is investigated.

The simulation parameters are listed in Table I. Specifically, we choose $P_{Tx} = 10$ dBm, $\gamma_{th} = 10$ dB, and $R_{th} = 10$ Gbps for the multi-path and 30 Gbps for the directional propagations. These parameter values are consistent with the state-of-art system and hardware design in the Terahertz band, in [7], [13], [14]. The feasible solutions are obtained by using these parameters.

Two types of pulses are used in the simulation for comparison. The pulse shapes are given by [18]

$$g_1(t) = \left(1 - \frac{25\pi t^2}{T_p^2}\right) e^{-12.5\pi t^2/T_p^2}, \quad (34)$$

$$g_2(t) = \frac{1}{\sqrt{T_p}}, \quad \text{for } -0.5T_p \leq t \leq 0.5T_p. \quad (35)$$

The pulses in the time domain and the frequency domain are plotted in Figs. 3(a) and 3(b), respectively. g_1 has a narrow time response and thus a wide frequency response. The bandwidth for g_1 is 10 GHz. In contrast, the rectangular pulse g_2

has the main lobe is 4 GHz wide and many sidelobes appear even at 20 GHz around the center frequency. The normalized power leakage values are 0.18% and 17.47% for the two pulses, respectively. This would cause the IBI in (14). Moreover, the auto-correlation functions of the two pulses are demonstrated in Fig. 3(c), whose values at mT_p are used in the computation of the ISI in (13).

A. SINR

By using (16) and (21), the SINR values for the different transmit power and the different number of frames are investigated. The observations are summarized as follows. First, the SINR increases with the transmit power and the number of frames, although the ISI and IBI rise at the same time. In Fig. 4(a), the SINR for the multi-path propagation at the distance of 5 m and at the sub-window of 60 GHz is shown. To reach the targeted signal strength requirement, for example $\gamma_{th} = 10$ dB, the possible solutions to the constraint (31) are $\{N_f^u = 1, P_u = 14$ dBm $\}$, $\{N_f^u = 10, P_u = 4$ dBm $\}$ and $\{N_f^u = 3, P_u = 9$ dBm $\}$.

Second, as the frequency increases, the THz band channel has higher path loss over the same distance. The resulting SINR reduces since the path gains decrease in the SINR express in (16), as shown in Fig. 4(b). To achieve the same signal strength, the minimum number of frame becomes 5 instead of 1 for the 60 GHz case, with the transmit power of 20 dBm. On the other hand, the minimum transmit power is 17 dBm instead of 9 dBm for the 60 GHz case, with the number of frames of 10. If the frequency further increases to 1 THz, $\gamma_{th} = 10$ dB cannot be satisfied for $d = 5$ m. Hence, Fig. 4(c) shows the SINR for $d = 1$ m, and the possible solutions to (31) are $\{N_f^u = 3, P_u = 19$ dBm $\}$, $\{N_f^u = 9, P_u = 14$ dBm $\}$ and $\{N_f^u = 7, P_u = 15$ dBm $\}$.

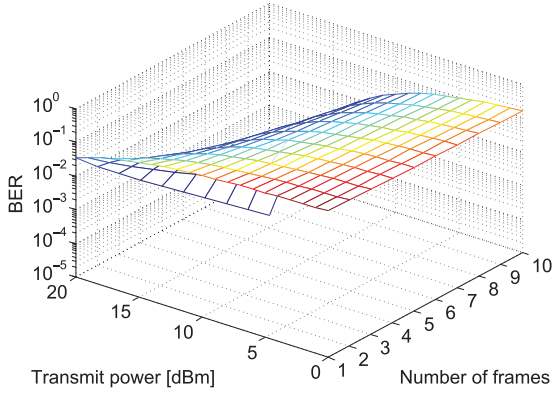


Fig. 5. BER for the multi-path propagation with $d = 5$ m, $f = 300$ GHz.

Third, with the use of the high-gain antennas, the SINR is greatly improved. In particular, when $G_t = G_r = 20$ dB, the communication distance can be enhanced to $d = 30$ m for $f = 0.3$ THz, as shown in Fig. 4(d). In the SINR expression in (21), the ISI is omitted since only the LoS path is considered for the directional transmission. Based on these parameter values, the SINR requirement is satisfied for the solutions $\{N_f^u = 1, P_u = 2$ dBm $\}$ and $\{N_f^u = 2, P_u = 0$ dBm $\}$, among others. Fourth, the influences of the transmit power and the number of frames are comparable. In particular, when the transmit power increases from 0 dBm to 10 dBm, the SINR value increases by 10 dB. This improvement of SINR is approximately the same if we send 10 frames instead of 1 frame for one symbol, as given in (4).

To maintain the required SINR, the tradeoff between the power efficiency and the rate effectiveness needs to be determined, since SINR is affected by the combination of the number of frames and the transmit power.

B. BER

Then, the BER is related to the SINR by using (23) and (24). The BER decreases with the increase of the SINR. Consequently, the BER decreases with the increase of the transmit power and the number of frames. To realize the error rate below 10^{-3} , the SINR needs to be greater or equal to 9 dB, while in particular, $\gamma_{\text{th}} = 10$ dB suggests $\text{BER} = 3.9 \times 10^{-4}$. For the multi-path propagation at 0.3 THz over 5 m, the BER is given in Fig. 5. A drastic decrease is observed for the BER and when N_f^u is no less than 4 and P_u is no less than 16 dBm, the BER is below 10^{-3} .

C. Power Allocation Schemes

By using the THz band channel and the waveform design, the rate is analyzed in this section. Four power allocation schemes are considered for $d = 1$ m and $P_{\text{Tx}} = 10$ dBm. The first scheme that minimizes power/bit allows an efficient utilization of the transmit power, as shown in Fig. 6(a). With the increase of the operating frequency, the path loss increases and the SINR decreases. To achieve the same power-per-bit, the allocated power increases steadily. More power is allocated to the higher frequency bands. The second scheme in Fig. 6(b) minimizes the number of frames over each sub-window. The transmit power is allocated only to the sub-windows with the small

carrier frequencies, i.e., up to 0.53 THz, while no power is provided for the higher frequency bands, which is equivalent to the truncated channel inversion scheme [22]. The third scheme follows the water-filling principle, which allocates more power to the sub-windows that have better SINR, as illustrated in Fig. 6(c). However, this scheme requires a feedback path to supply the channel information at the transmitter [10], which is very costly since the channel variation can be very fast over time at THz frequencies due to the mobility or the transmission medium changes. The fourth schemes allocates the transmit power equally over the sub-windows from 0.06 THz to 1 THz, as shown in Fig. 6(d). This scheme allows the offline allocation of the transmit power and consequently the number of frames.

D. Achievable Rates

The total rate over the 0.06-1 THz band for the multi-path propagation is analyzed for the aforementioned four power allocation schemes with $P_{\text{Tx}} = 10$ dBm, as shown in Fig. 7(a). When the distance is below 4 m, the equal-power scheme outperforms the others and requires no channel information. However, the decreasing rate of this scheme is the largest. The first scheme and the water-filling scheme have very close performance until $d = 5$ m. Above this distance, the path loss and the frequency selectivity degrade significantly as shown in Fig. 1(a). As a result, the first scheme has the largest throughput since it has the most efficient utilization of the transmit power over the 0.06-1 THz band. In contrast, the second scheme allocates the transmit power up to 0.25 THz (see Fig. 6(b)), and has the worst rate performance among the four schemes. Quantitatively, at $d = 1$ m, the rate values for the four schemes are 18.2 Gbps, 11.6 Gbps, 20.1 Gbps, and 27.3 Gbps, respectively. Furthermore, the decreasing rates for the four schemes are approximated as 1.67 Gbps/m, 1.02 Gbps/m, 2.06 Gbps/m, and 3.00 Gbps/m, separately, from 1 m to 10 m.

In addition to the multi-path propagation, we analyze the rate for the directional transmission case, by exploiting the spectral windows discussed in Section II-B2. Surprisingly, the rate performance of the first scheme that minimizes $P_u \cdot N_f^u$ degrades significantly and is the worst among others. This is due to the fact that the first scheme allocates more power to the sub-windows that have worse attenuations, as shown in Fig. 6(a). This power allocation scheme performs well for the multi-path propagation, when the SINR at the receiver is low. However, for the directional transmission at 20 m, this scheme uses 16.06 dBm of the total power, which is 4.3% of P_{Tx} . The underexploited use of the transmit power leads to the severe rate degradation of this scheme. On the contrary, the other three schemes take the advantages of the antenna gains, (i.e., $G_t = G_r = 20$ dB). The rate and the communication distance are significantly enhanced. Fig. 7(b) shows the rate over the distance up to 50 m. The min N_f , water-filling and equal-power schemes perform approximately the same in this case. However, the equal-power scheme allows the offline computation of the transmit power and hence the number of frames. As a result, the equal-power scheme is desired for the directional transmission.

In Fig. 8, the rate values are evaluated for the different mean transmit power, P_{Tx} , in (30), by adopting the first power allocation scheme in the multi-path propagation. The decreasing rates

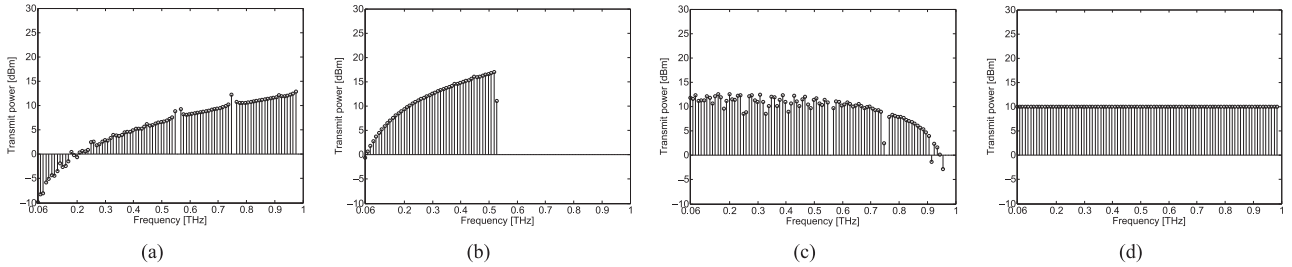


Fig. 6. Transmit power over the 0.06–1 THz spectrum for the different allocation schemes, with $d = 1$ m, $P_{T_x} = 10$ dBm. (a) Min power/bit. (b) Min N_f . (c) Water-filling. (d) Equal-power.

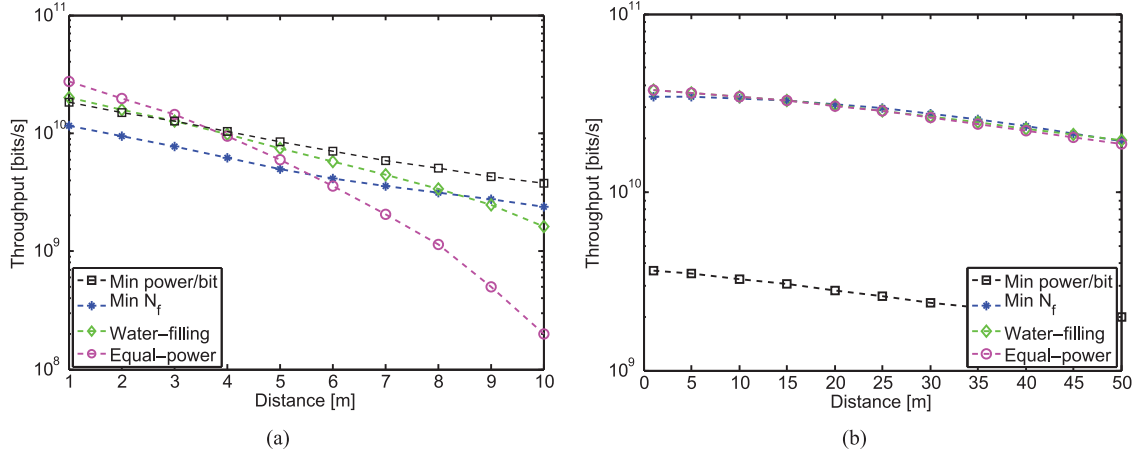


Fig. 7. Data rates for the different allocation schemes over 0.06–1 THz band, and $P_{T_x} = 10$ dBm. (a) Multi-path propagation. (b) Directional transmission.

of the rate are comparable for the different transmit power. In particular, the average rate over the distance 1 m to 10 m is 9.07 Gbps, when the mean transmit power is 10 dBm. The rate values reduce by 29.0% and 50.5%, to 6.44 Gbps, and 4.49 Gbps, when the transmit power changes to 5 dBm and 1 dBm, respectively. If we use g_2 , due to the increase of the ISI and IBI, the rate by using the rectangular pulse is slightly worse than g_1 . In particular, the average rates are 9.00 Gbps, 6.39 Gbps and 4.41 Gbps for the given transmit power. From this analysis, the pulse type makes insignificant influence on the system performance.

E. Distance Improvement

Based on the analysis on the wideband signal model, the SINR, and dynamic allocation of the power and the number of frames, we obtain the solutions to the optimization problem in Section IV-B. By using the four allocation schemes, the maximum distances that can be supported are shown in Fig. 9(a) for the multi-path propagation, and in Fig. 9(b) for the directional transmission, respectively. With the transmit power $P_{T_x} = 10$ dBm, the largest distance to support $R_{th} = 10$ Gbps for the multi-path propagation is 4 m, which is realized via the first allocation scheme. As seen in Fig. 9(a), the scheme to minimize power-per-bit outperforms than the other three allocation schemes, except when $P_{T_x} = 1$ dBm, the second scheme to minimize the number of frames can reach the largest distance of 1.28 m. Compared to the fixed power scheme, the distance is improved by 25% for 1 dBm and 2.6% for 10 dBm.

On the other hand, when the high-gain antennas are used, the first scheme that minimizes power-per-bit under-exploits the

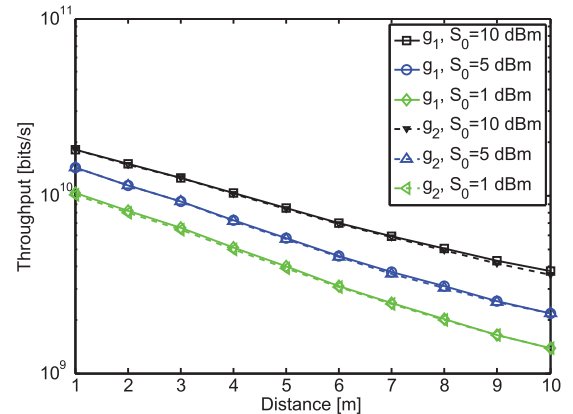


Fig. 8. Data rates for the different transmit power and waveforms. The min power/bit scheme is used in the multi-path propagation.

transmit power severely. Instead, the other three schemes have comparable performances and the second scheme that minimizes the number of frames slightly outperforms. In terms of the maximum distance that achieves $R_{th} = 30$ Gbps, the second scheme reaches 22.5 m when $P_{T_x} = 10$ dBm. This coverage reduces with the transmit power, and drops to 10 m when $P_{T_x} = 1$ dBm. Although the equal-power scheme achieves 5%–10% less distance than the water-filling and the min N_f schemes, it has the lowest complexity by allowing the offline power allocation and rate computation.

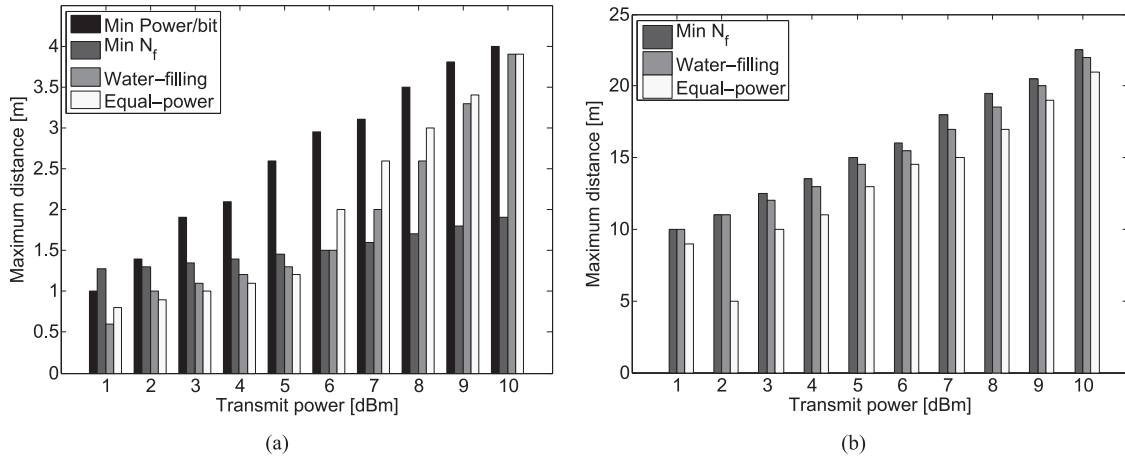


Fig. 9. Maximum distance for the different transmit power, over 0.06–1 THz band. (a) $R_{th} = 10$ Gbps for the multi-path propagation. (b) $R_{th} = 30$ Gbps for the directional transmission. The min power/bit scheme under-exploits the transmit power severely and is excluded for comparison.

VI. CONCLUSION

In this paper, we proposed a multi-wideband waveform design for the THz band, which includes the features of the pseudo-random time-hopping sequence and the polarity randomization, and allows the dynamical variation of the rate and the transmit power on each sub-window. Moreover, we derived the ISI and the IBI and provided the closed-form expressions of the SINR and BER for the developed multi-wideband waveform. Based in the system model and the waveform design, we formulated an optimization framework to solve for the multi-wideband waveform design parameters of the transmit power and the number of frames, with the aim to maximize the communication distance while satisfying the rate and the transmit power constraints. Four sub-optimal solutions are proposed and compared via extensive numeral analysis.

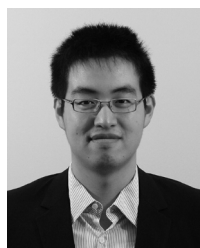
The results showed that the SINR increase with the transmit power and the number of frames in the multi-wideband waveform design, at the cost of the consumption of the power and the decrease of the rate. With the transmit power of 10 dBm, the largest distance to support 10 Gbps for the multi-path propagation is 4 m, which is realized via the power allocation scheme to minimize the power/bit on each sub-window and is 10% improvement over the fixed scheme. However, for the directional transmission, this scheme under-exploits the transmit power severely. Instead, the allocation scheme that minimizes the number of frames outperforms. In terms of the maximum distance that achieves 30 Gbps, this scheme reaches 22.5 m. Although the equal-power scheme achieves 5%–10% less distance than the water-filling and the min N_f schemes, it has the lowest complexity by allowing the offline power allocation and rate computation.

The future work may include the joint design of modulation and coding for the multi-wideband communication in the THz band, to further improve the SINR and the distance. Moreover, a tailored medium access control scheme based on the proposed pulse waveform design is attractive. Furthermore, a resource allocation scheme can be developed, which captures the peculiarities of distance-varying spectral windows and efficiently exploits the Terahertz spectrum.

REFERENCES

- [1] H. Song and T. Nagatsuma, "Present and future of terahertz communications," *IEEE Trans. THz Sci. Technol.*, vol. 1, no. 1, pp. 256–263, 2011.
- [2] T. Kleine-Ostmann and T. Nagatsuma, "A review on terahertz communications research," *J. Infrared, Millimeter and Terahertz Waves*, vol. 32, pp. 143–171, 2011.
- [3] I. F. Akyildiz, J. M. Jornet, and C. Han, "TeraNets: Ultra-broadband communication networks in the terahertz band," *IEEE Wireless Commun. Mag.*, vol. 21, no. 4, pp. 130–135, Aug. 2014.
- [4] T. Kürner and S. Priebe, "Towards THz communications-status in research, standardization and regulation," *J. Infrared, Millimeter, and Terahertz Waves*, pp. 1–10, 2013.
- [5] I. F. Akyildiz, J. M. Jornet, and C. Han, "Terahertz band: Next frontier for wireless communications," *Phys. Commun. J.*, vol. 12, pp. 16–32, Mar.–Jun. 2014.
- [6] J. M. Jornet and I. F. Akyildiz, "Graphene-based plasmonic nano-antenna for terahertz band communication in nanonetworks," *IEEE J. Sel. Areas Commun., Special Issue on Emerging Technologies for Commun.*, vol. 31, no. 12, pp. 685–694, 2013.
- [7] C. Han, A. O. Bicen, and I. F. Akyildiz, "Multi-ray channel modeling and wideband characterization for wireless communications in the terahertz band," *IEEE Trans. Wireless Commun.*, vol. 14, no. 5, pp. 2402–2412, 2015.
- [8] C. Lin and G. Y. Li, "Indoor terahertz communications: How many antenna arrays are needed?," *IEEE Trans. Wireless Commun.*, vol. 14, no. 6, p. 30973107.
- [9] J. M. Jornet and I. F. Akyildiz, "Femtosecond-long pulse-based modulation for terahertz band communication in nanonetworks," *IEEE Trans. Commun.*, vol. 62, no. 5, pp. 1742–1754, 2011.
- [10] C. Han and I. F. Akyildiz, "Distance-aware multi-carrier (DAMC) modulation in terahertz band communication," in *Proc. IEEE Int. Conf. Commun. (ICC)*, 2014.
- [11] S. Gezici, Z. Sahinoglu, H. Kobayashi, and H. V. Poor, "Ultra-wideband impulse radio systems with multiple pulse types," *IEEE J. Sel. Areas Commun.*, vol. 24, no. 4, pp. 892–898, 2006.
- [12] Y.-P. Nakache and A. F. Molisch, "Spectral shape of UWB signals-influence of modulation format, multiple access scheme and pulse shape," in *Proc. IEEE Veh. Technol. Conf.*, 2003, vol. 4, pp. 2510–2514.
- [13] T. Schneider, A. Wiatrek, S. Preußler, M. Grigat, and R.-P. Braun, "Link budget analysis for terahertz fixed wireless links," *IEEE Trans. THz Sci. Technol.*, vol. 2, no. 2, pp. 250–256, 2012.
- [14] C. Zhang, C. Han, and I. F. Akyildiz, "Three dimensional end-to-end modeling and directivity analysis for graphene-based antennas in the terahertz band," in *Proc. IEEE Global Telecommun. Conf., GLOBECOM*, 2015.
- [15] W. D. Wu, C. C. Lee, C. H. Wang, and C. C. Chao, "Signal-to-interference-plus-noise ratio analysis for direct-sequence ultra-wideband systems in generalized Saleh-Valenzuela channels," *IEEE J. Sel. Topics Signal Process.*, vol. 1, no. 3, pp. 483–497, 2007.

- [16] T. Keller and L. Hanzo, "Adaptive multicarrier modulation: A convenient framework for time-frequency PROCESSING in wireless communications," *Proc. IEEE*, vol. 88, no. 5, pp. 611–640, 2000.
- [17] K. Sathananthan and C. Tellambura, "Probability of error calculation of OFDM systems with frequency offset," *IEEE Trans. Commun.*, vol. 49, no. 11, pp. 1884–1888, 2001.
- [18] S. Gezici, H. Kobayashi, H. V. Poor, and A. F. Molisch, "Performance evaluation of impulse radio UWB systems with pulse-based polarity randomization," *IEEE Trans. Signal Process.*, vol. 53, no. 7, pp. 2537–2549, 2005.
- [19] A. Rajeswaran, V. S. Somayazulu, and J. R. Foerster, "Rake performance for a pulse based UWB system in a realistic UWB indoor channel," in *Proc. IEEE Int. Conf. Commun., ICC.*, 2003, vol. 4, pp. 2879–2883.
- [20] H. Liu, "Error performance of a pulse amplitude and position modulated ultra-wideband system over lognormal fading channels," *IEEE Commun. Lett.*, vol. 7, no. 11, pp. 531–533, 2003.
- [21] C. Y. Wong, R. S. Cheng, K. B. Lataief, and R. D. Murch, "Multiuser OFDM with adaptive subcarrier, bit, and power allocation," *IEEE J. Sel. Areas Commun. (JSAC)*, vol. 17, no. 10, pp. 1747–1758, 1999.
- [22] H. ElSawy and E. Hossain, "On stochastic geometry modeling of cellular uplink transmission with truncated channel inversion power control," *IEEE Trans. Wireless Commun.*, vol. 13, no. 8, pp. 4454–4469, 2014.
- [23] D. Cassioli, M. Z. Win, F. Vatalaro, and A. F. Molisch, "Performance of low-complexity Rake reception in a realistic UWB channel," in *Proc. IEEE Int. Conf. Commun., ICC*, 2002, vol. 2, pp. 763–767.



Chong Han (S'12) received the Bachelor of Engineering degree in Electrical Engineering and Telecommunications from The University of New South Wales, Sydney, Australia, in 2011, and received the Master of Science degree in Electrical and Computer Engineering from Georgia Institute of Technology, Atlanta, USA, in 2012. Currently, he is a graduate research assistant in the Broadband Wireless Networking Laboratory (BWN Lab), School of Electrical and Computer Engineering, Georgia Institute of Technology. He is pursuing his Ph.D.

degree under the supervision of Prof. Ian F. Akyildiz. His current research interests include Terahertz band communication networks, Millimeter-wave

systems, 5G Cellular Networks, Internet of Things, Internet of Nano-Things, and Electromagnetic Nanonetworks.



communication.

A. Ozan Bicen (S'08) received the B.Sc. and M.Sc. degrees in Electrical and Electronics Engineering from Middle East Technical University, Ankara, Turkey, in 2010 and from Koc University, Istanbul, Turkey, in 2012, respectively. He is currently a Graduate Research Assistant in the Broadband Wireless Networking Laboratory and pursuing his Ph.D. degree at the School of Electrical and Computer Engineering, Georgia Institute of Technology, Atlanta, GA. His current research interests include wireless communication at the THz band, and molecular



Ian F. Akyildiz (M'86–SM'89–F'96) received the B.S., M.S., and Ph.D. degrees in Computer Engineering from the University of Erlangen-Nurnberg, Germany, in 1978, 1981 and 1984, respectively. Currently, he is the Ken Byers Chair Professor in Telecommunications with the School of Electrical and Computer Engineering, Georgia Institute of Technology, Atlanta, the Director of the Broadband Wireless Networking Laboratory and Chair of the Telecommunication Group at Georgia Tech. Dr. Akyildiz is an honorary professor with the School of Electrical Engineering at Universitat Politècnica de Catalunya (UPC) in Barcelona, Catalunya, Spain and founded the N3Cat (NaNoNetworking Center in Catalunya). Since September 2012, Dr. Akyildiz is also a FiDiPro Professor (Finland Distinguished Professor Program (FiDiPro) supported by the Academy of Finland) at Tampere University of Technology, Department of Communications Engineering, Finland. He is the Editor-in-Chief of *Computer Networks* (Elsevier) journal, and the founding Editor-in-Chief of the *Ad Hoc Networks* (Elsevier) journal, the *Physical Communication* (Elsevier) journal and the *Nano Communication Networks* (Elsevier) journal. He is an ACM Fellow (1997). He received numerous awards from IEEE and ACM. His current research interests are in Terahertz band communication, nanonetworks, software defined networking, 5G cellular systems and wireless underground sensor networks.